13 Phase transitions and superconducting photon detectors

A. Aeschbacher, F. von Rohr, H. Grundmann, O. Bossen, K. Inderbitzin, S. Siegrist, A. Engel and A. Schilling

in collaboration with: University of Bern (K. Krämer), EPF Lausanne (L. Forró), Tohoku University (N. Toyota), McMaster University (H. Dabkowska), Karlsruhe Institut für Technologie (K. Il'in), ETH Zürich (A. Imamoglu), Deutsches Zentrum für Luft- und Raumfahrt (H.-W. Hübers, A. Semenov), FIRST Lab ETH Zürich, ESRF Grenoble (C. Mazzoli), PSI Villigen (M. Medarde).

13.1 Superconducting nanowire single-photon detectors for optical and X-ray photons

In this report period we could demonstrate that it is possible to make fast single-photon detectors from TaN, which show improved detection efficiencies in the infrared spectral range compared to traditional detectors made from NbN. Moreover, in experiments with X-rays ($\approx 6-50$ keV) we successfully transferred the detection principle into the keV region while preserving the fast recovery times.

13.1.1 TaN superconducting nanowire single-photon detectors

In the previous annual report we already reported preliminary results of superconducting nanowire single-photon detectors (SNSPD) sensitive in the optical and near-infrared range made from TaN thin films [1] instead of the common NbN material. These efforts were motivated by the expectation that materials with a lower critical temperature T_c compared to NbN should detect low-energy photons in the infrared with a higher detection efficiency. An extensive and detailed comparison with a similar sized NbN-SNSPD confirmed our expectations [2]. At high bias currents the detection efficiency as a function of the photon wavelength λ shows a well defined plateau extending well into the infrared range followed by the typical roll-off beyond the cut-off wavelength (Fig. 13.1). The improvement compared to a similarly sized NbN SNSPD becomes obvious when the relative detection efficiency $\mathrm{DE_{TaN}/DE_{NbN}}$ for equal reduced bias current I_b/I_c is plotted versus λ as shown in the inset of Fig. 13.1. For $\lambda > 1100$ nm the detection efficiency of the TaN detector is 5 to 6 times higher than for the NbN detector.

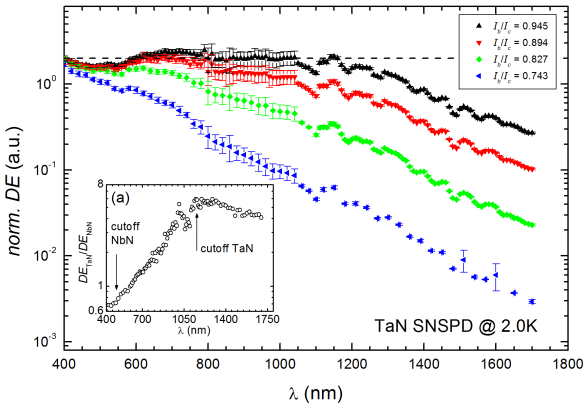

FIG. 13.1 – *Detection efficiency of the TaN SNSPD as a function of photon wavelength for different bias currents. In the inset we plotted the relative detection efficiencies for a TaN and NbN detector. The 5 to 6-fold increase of the detection efficiency in the infra-red is clearly visible.*

This improvement has been achieved without compromise in the speed of the detector—its main advantage compared to competing technologies. In Fig. 13.2 voltage traces recorded for both detectors are shown. The pulses are almost identical for both detectors. Especially the rise time is for both detectors $\sim$ 200 ps, given by the 2 GHz bandwidth of our readout electronics. This is already indicating a very small timing jitter for the detection of photons, important for time-correlation experiments. This was confirmed by time-correlation measurements in a setup in the group of Prof. Imamoglu at ETH Zürich, from which we could determine a timing jitter of $\sim$ 80 ps, comparable to standard NbN SNSPD.

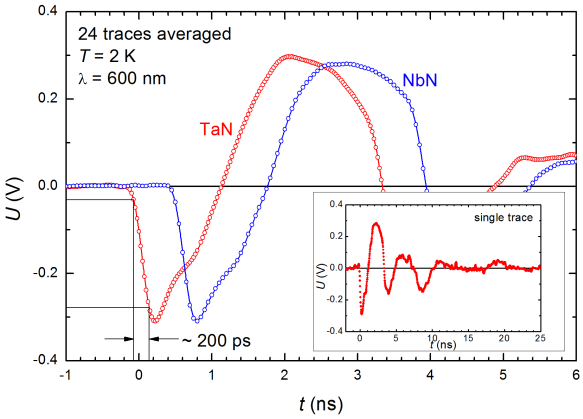

FIG. 13.2 – *Amplified and scaled voltage traces of photon counts. In the main figure voltage traces averaged over 24 individual events for a TaN SNSPD (red) and a reference NbN SNSPD (blue) are plotted as a function of time. The rise time of about 200 ps is about the same for both detectors and effectively given by the 2 GHZ bandwidth of our readout electronics. The inset shows a longer time interval for a single trace.*

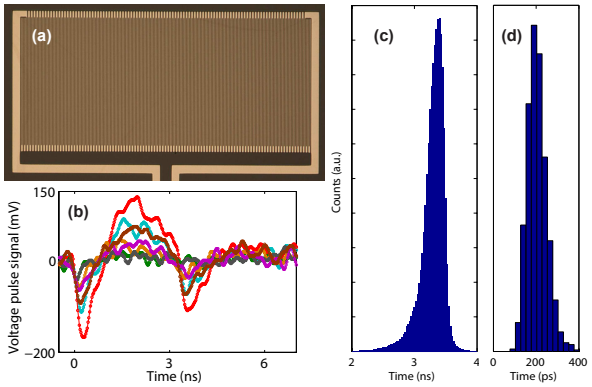

FIG. 13.3 – *(a) Optical image of examined X-SNSPD from 100 nm thick niobium, (b) typical voltage pulses after X-ray photon absorption, (c) pulse length histogram and (d) pulse rise time histogram (time spans between 15% and 85% of voltage minimum)*

13.1.2 X-ray superconducting nanowire single-photon detectors

More than a decade before the successful development of SNSPD for the optical and near-IR wavelength range, serious efforts were undertaken to use this detection principle for X-ray photons with keV-energies [3]. However, these preliminary X-ray detectors struggled with problems after photon detection, making it difficult to operate them in a continuous detection mode. Recently, SNSPDs were used in time-of-flight spectrometry of molecules [4]. For this purpose, a SNSPD from 5 nm thin NbN was successfully tested for X-ray detection in a feasibility study [5]. However, the absorptivity of thin NbN films for X-ray photons and therefore the quantum efficiency of the detectors, are low.

In order to enhance the absorptivity of the superconducting detector, we fabricated an X-ray superconducting nanowire single-photon detector (X-SNSPD) from 100 nm thick niobium (Fig. 13.3a). The detector geometry was designed for a kinetic inductance large enough to significantly reduce the above mentioned problem with continuous photon detection, and small enough for ultrafast pulse recovery times. We report on the detection of X-ray photons with keV-energies with an ultrafast pulse recovery time of less than 4 ns (Fig. 13.3b and c) and an average pulse rise time of about 200 ps (Fig. 13.3d), again limited only by our electronics setup. In contrast to optical photon-detection in thin-film SNSPDs, X-ray photon detection was possible even at bias currents smaller than 1% of the critical current.

Most remarkably, we observed that the average X-SNSPD signal amplitude depends significantly on the acceleration voltage of the photon emitting X-ray tube. Figure 13.4 shows the corresponding normalized pulse amplitude histograms at different acceleration voltages between 6 kV and 50 kV. Since the detector operates in a single-photon detection mode (inset Fig. 13.4), the variation of the average signal amplitude can be attributed to the variation of the average photon energies at different X-ray tube settings. This phenomenon, which is new for SNSPDs, is explained by the orders-of-magnitude smaller resistance of the normal conducting domains as compared to the situation in thin-film SNSPDs.

Moreover, no dark count events were triggered in over four hours of measurement, even with bias currents very close to the critical current.

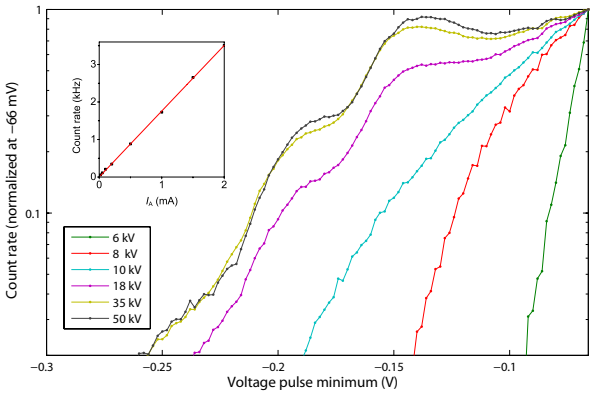

FIG. 13.4 – *Histograms of voltage pulse minima for different X-ray tube acceleration voltages (indicated in the legend). The acceleration voltage determines the maximum energy of the emitted photons. The inset shows that the detector photon count rate is proportional to the photon flux, which was varied by the X-ray tube anode current.*

Our results show that ultrafast dark-count-free X-SNSPDs can be fabricated which can operate in a large spectral range. They could find applications where very high count rates, precise timing, a good signal-to-noise ratio and response in a wide spectral range for photon counting are required.

13.2 Experiments on $Ba_{3-x}Sr_xCr_2O_8$

We have revived an old idea (see, e.g., JB 2006/07) to examine possibilities to directly prove the existence or the absence of macroscopic phase coherence in a condensate of triplon quasiparticles. We have realized that the time scale for a corresponding measurement is determined by the expected lifetime of phase coherence and was chosen much too long in earlier corresponding magnetic resonance experiments [6].

In an alternative approach we have recently suggested that two interacting triplon condensates with different chemical potentials (i.e. critical fields H_c) should show an a.c. Josephson effect (similar to that observed in superconducting junctions) if they are placed into a common external magnetic field exceeding both critical fields. This effect would manifest itself in a change in the respective energy spectra. To account for the limited quasiparticle lifetime ($> 10^{-11}$ s [6]) we expect a corresponding experiment to be successful in a junction composed of two weakly coupled compounds with critical fields $\mu_0 H_c$ differing by at least 0.5 T, and with a low enough intrinsic exchange-interaction anisotropy ($< 4\,\mu$eV). As a result of the coupling, certain ESR (electron-spin resonance) active modes should split enough to be observable [6] (i.e., by $\omega_{\text{a.c.}} \approx 10^{11}\,\text{s}^{-1}$), which can be investigated in a corresponding high-resolution ESR experiment.

13.2.1 Synthesis of $Ba_{3-x}Sr_xCr_2O_8$ as a prototype material

As a first preliminary study we have attempted to synthesize samples within the solid solution $Ba_{3-x}Sr_xCr_2O_8$. The reason for this choice is *a)* the relatively low exchange-interaction anisotropy of $Ba_3Cr_2O_8$ and $Sr_3Cr_2O_8$ ($\approx 1\,\mu$eV), *b)* the relatively low critical field of $Ba_3Cr_2O_8$ ($\mu_0 H_c \approx 12$ T [7], which is accessible in standard superconducting laboratory magnets), and *c)* the existence of isostructural $Sr_3Cr_2O_8$ with a $\mu_0 H_c \approx 30$ T [8]. Up to now, the solid solution $Ba_{3-x}Sr_xCr_2O_8$ has not yet been reported in the literature, and our aim was not only to show that it exists, but also to explore its physical properties later on.

These synthesis experiments where carried out by the PhD student Henrik Grundmann at the UZH and at McMaster University in Hamilton, Canada, with the help of Dr. Hanna Dabkowska. Although these experiments in an optical floating zone furnace did not yield strictly single-crystalline samples, the re-solidified material contained several, relatively large, well oriented crystallites, which was confirmed by Laue diffraction experiments.

The lattice constants were estimated from the Debye-Scherrer-spectra of reground crystallites (see Fig. 13.5 for a comparison of simulated Debye-Scherrer spectra for $Ba_3Cr_2O_8$ and $Sr_3Cr_2O_8$ with experimental data for $Ba_{1.5}Sr_{1,5}Cr_2O_8$). The numerical values listed in Tab. 13.1 are close to what is expected according to Vegards law, based on the lattice constants of $Ba_3Cr_2O_8$ [7] and $Sr_3Cr_2O_8$ [8]. A more precise structural refinement of all prepared compounds is in progress.

TAB. 13.1 – Lattice parameters a and c^a of the prepared $Ba_{3-x}Sr_xCr_2O_8$ samples.

material	literature value		from powder spectra		expected from Vegards law	
	a	c	a	c	a	c
$Ba_3Cr_2O_8$	5.742 Å	21.389 Å[7]	-	-	-	-
$Ba_{2.9}Sr_{0.1}Cr_2O_8$	-	-	5.709 Å	21.367 Å	5.734 Å	21.350 Å
$Ba_{1.5}Sr_{1.5}Cr_2O_8$	-	-	5.67 Å	20.8 Å	5.5613 Å	20.805 Å
$Sr_3Cr_2O_8$	5.562 Å	20.221 Å[8]	-	-	-	-

[a] notation according to Ref. [8]

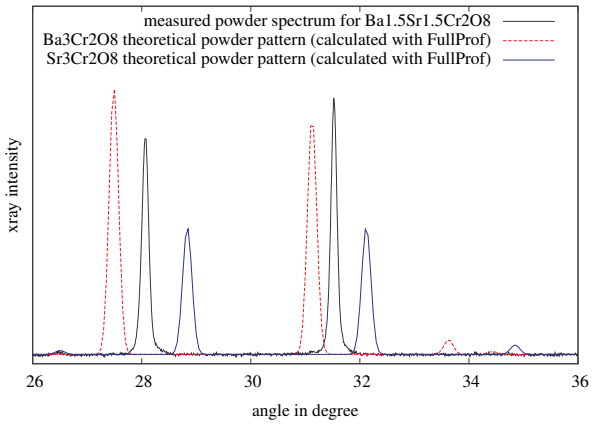

FIG. 13.5 – *Comparison of Debye-Scherrer measurements for $Ba_{1.5}Sr_{1.5}Cr_2O_8$ with simulated powder spectra for $Ba_3Cr_2O_8$ and $Sr_3Cr_2O_8$.*

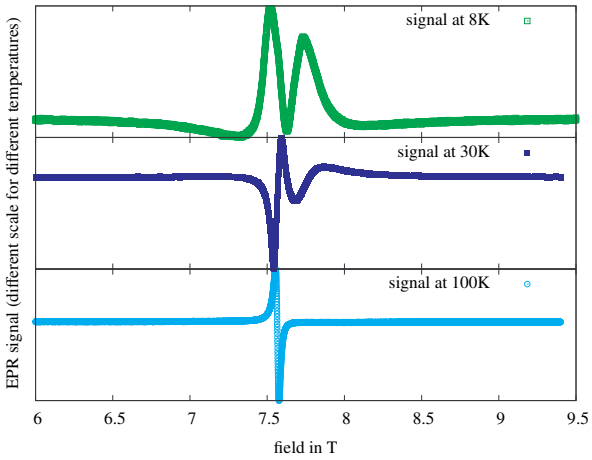

FIG. 13.6 – *EPR signal (ν=210 GHz) at different temperatures.*

13.2.2 Investigation of the ESR/EPR linewidths in $Ba_3Cr_2O_8$

In a second preliminary study we wished to examine whether the intrinsic line widths in the high-field EPR spectra of $Ba_{3-x}Sr_xCr_2O_8$ would allow for the detection of the expected line splitting or not. Measurements on powdered $Ba_3Cr_2O_8$ were carried out at the high-field EPR setup in the group of Prof. László Forró at the EPFL, Lausanne. We found that the width of the ESR line corresponding to transitions between neighbouring triplet branches in $\nu = 210$ GHz is smaller than 0.2 T below room temperature (see Fig. 13.6, lowest panel). Therefore, from the instrumental point of view, it should be possible in principle to detect a line splitting of 0.5 T in this material.

However, below T$\approx$ 80 K, an additional line showed up (see Fig. 13.6, upper panels), with an intensity that increases with decreasing temperature. Up to now it is not clear if this can be attributed to a structural phase transition that occurs around this temperature [9] or if it is due to another phenomenon. We will perform additional EPR measurements on single crystalline samples of $Ba_3Cr_2O_8$ and the solid solutions $Ba_{3-x}Sr_xCr_2O_8$ to clarify this issue.

13.3 *LC*-circuit calorimetry

In conventional calorimetric a.c. methods, a heat capacity is calculated from the amplitude of an imposed temperature oscillation. It is known that the statistical error of such a measurement decreases with measuring time t as $t^{-1/2}$. If an oscillator could be built in which the heat capacity C acts like an electrical capacitance together with a known electrical inductance L, C could be calculated from the resulting resonance frequency ω according to

$C = 1/(L\omega^2)$. Alternatively, L could be a (hypothetical) "thermal inductor". Rife and Boorstyn [10] have shown that the measurement error for frequency measurements under white noise conditions depends on the measuring time as $t^{-3/2}$, as opposed to $t^{-1/2}$ for measurements of the amplitude. Therefore, a device measuring a frequency that is determined by the heat capacity would maintain most of the advantages of all other a.c.-calorimetry-methods, but the accuracy would be greatly improved.

We have successfully constructed such a device in our laboratory with an "effective thermal inductance" by using Peltier elements connected to an electrical inductance L. When the Peltier elements are coupled to a sample and equipped with suitable amplification, we reach autonomous LC-circuit oscillations with a frequency that depends on the heat capacity C as

$$\omega = \frac{1}{\sqrt{\Pi\alpha LC}}, \qquad (13.1)$$

where Π and α are the Peltier and Seebeck coefficients of the Peltier element, respectively.

The detailed electrical set up is shown in Fig. 13.7. An inductance of $L \approx 10$ H is realized in the form of an electrical gyrator circuit. The sample is sandwiched between two Peltier elements placed inside a PPMS cryostat (Physical Property Measurement System, Quantum Design Inc.), to control the temperature and magnetic field. The first Peltier element essentially converts variations in the thermal current into corresponding changes in an electrical current. This induces a voltage across L that creates a temperature difference at the Peltier element, thereby counteracting the thermal current. The element is therefore acting as an "effective thermal inductor". The second sensing Peltier element is used together with an amplifier to provide compensation for electrical and thermal losses.

The performance of the setup was verified with a sample of 45.2 mg of Gadolinium, a ferromagnet with a Curie temperature of $T_C \approx 290$ K. We show in Fig. 13.8(a) the oscillation frequency of the thermal LC circuit that varies with temperature, together with the calculated heat capacity

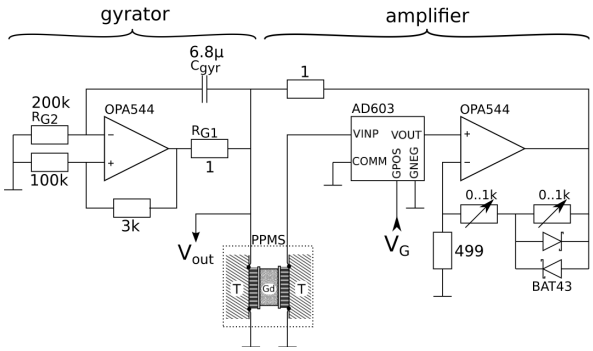

FIG. 13.7 – *Schematic of the oscillator circuit. On the left side an electrical gyrator of $L \approx 10$ H forms a resonant circuit with the Gd sample coupled through a Peltier element, while the right side acts as an amplifier to compensate for electrical and thermal losses.*

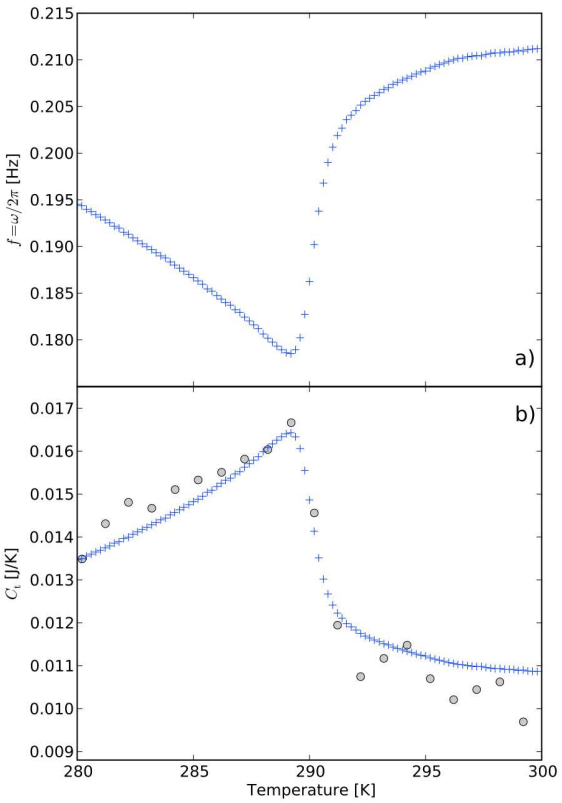

FIG. 13.8 – *a) Frequency of the thermal oscillations and b) calculated heat capacity of the test sample (both blue), compared with heat capacity data of the same sample measured with a commercial PPMS option (grey circles).*

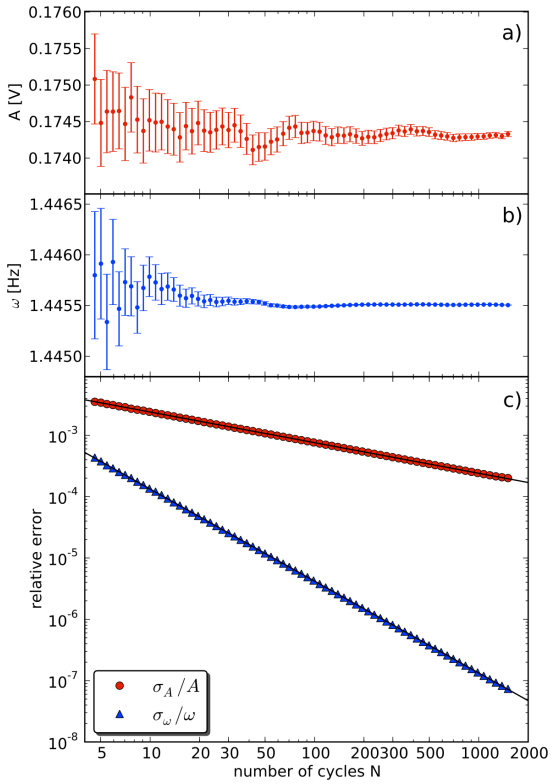

FIG. 13.9 – *Results of fits to data taken for an increasing number of measurement cycles N (*i.e., *increasing measuring time t) for a selected data point from Fig. 13.8. The statistical error in the amplitude A of the temperature oscillation decreases as $N^{-1/2}$, while the corresponding error in frequency and therefore in C decreases as $N^{-3/2}$ as expected.*

(Fig. 13.8(b)) in comparison with the data obtained from the commercial heat-capacity option of the PPMS. A plot of the statistical errors of amplitude A and frequency ω obtained from Levenberg-Marquardt fits to the respective temperature oscillations confirms the theoretical predictions for the evolution of the statistical errors with time (see Fig. 13.9) [11, 12].

Autonomous temperature oscillations have now been achieved down to 87 K, thereby demonstrating the feasibility of this technique also at lower temperatures. It remains to be seen, however, if sufficient accuracy improvements and robustness to noise in "vortex-shaking" experiments can be achieved to perform measurements on superconductors and at even lower temperatures.

[1] K. Il'in *et al.*, published online in J. Low Temp. Phys., (2011) http://dx.doi.org/10.1007/s10909-011-0424-3.

[2] A. Engel *et al.*, Appl. Phys. Lett., 100 (2012) 062601

[3] A. Gabutti *et al.*, Nucl. Instrum. Methods A, 278 (1989) 425-430; ibid., 312 (1992) 475-482; L. Parlato *et al.*, Nucl. Instrum. Methods A, 348 (1994) 127-130.

[4] K. Suzuki *et al.*, J. Low Temp. Phys., 151, (2008) 766-770; K. Suzuki *et al.*, Appl. Phys. Express, 1, (2008) 031702; N. Zen *et al.*, Appl. Phys. Letters, 95, (2009) 172508.

[5] D. Perez de Lara *et al.*, J. Low Temp. Phys., 151, (2008) 771-776.

[6] A. Schilling *et al.*, accepted by J. Phys.: Conf. Ser., http://arxiv.org/abs/1107.4335; A. Schilling and H. Grundmann, accepted by Ann. Phys. (NY), http://arxiv.org/abs/1101.1811

[7] A. A. Aczel *et al.*, Journal of Crystal Growth, 310 (2008) 870; M. Kofu *et al.*, Phys. Rev. Lett., 102 (2009) 177204.

[8] E. Cuno and H. Müller-Buschbaum, Z. anorg. allg. Chemie, 572 (1989) 95; A. A. Aczel *et al.*, Phys. Rev. Lett., 103 (2009) 207203.

[9] M. Kofu *et al.*, Phys. Rev. Lett., 102 (2009) 037206.

[10] D. C. Rife and R. R. Boorstyn, IEEE Trans. Inf. Theory IT-20, (1974) 591.

[11] O. Bossen and A. Schilling, Rev. Sci. Instrum., 82 (2011) 094901.

[12] Nature Physics, 7, (2011) 743.